



HAL
open science

Observation of >5 wt % zinc at the Kimberley outcrop, Gale crater, Mars

J. Lasue, S. M. Clegg, O. Forni, A. Cousin, R. C. Wiens, N. Lanza, N. Mangold, Laetitia Le Deit, O. Gasnault, S. Maurice, et al.

► To cite this version:

J. Lasue, S. M. Clegg, O. Forni, A. Cousin, R. C. Wiens, et al.. Observation of >5 wt % zinc at the Kimberley outcrop, Gale crater, Mars. *Journal of Geophysical Research. Planets*, 2016, 10.1002/2015JE004946 . hal-01302528

HAL Id: hal-01302528

<https://hal.univ-lorraine.fr/hal-01302528>

Submitted on 4 Jan 2022

HAL is a multi-disciplinary open access archive for the deposit and dissemination of scientific research documents, whether they are published or not. The documents may come from teaching and research institutions in France or abroad, or from public or private research centers.

L'archive ouverte pluridisciplinaire **HAL**, est destinée au dépôt et à la diffusion de documents scientifiques de niveau recherche, publiés ou non, émanant des établissements d'enseignement et de recherche français ou étrangers, des laboratoires publics ou privés.

Copyright

RESEARCH ARTICLE

10.1002/2015JE004946

Special Section:

The Mars Science Laboratory Rover Mission (Curiosity) at The Kimberley, Gale Crater, Mars

Key Points:

- Zinc-enriched targets have been detected at the Kimberley outcrop using ChemCam
- A dedicated database and model have been developed for quantification
- Possible origin: supergene sphalerite gossan cap alteration or hypogene nonsulfide zinc deposition

Supporting Information:

- Figures S1–S3 and Table S1
- Table S2

Correspondence to:

J. Lasue,
jlasue@irap.omp.eu

Citation:

Lasue, J., et al. (2016), Observation of > 5 wt % zinc at the Kimberley outcrop, Gale crater, Mars, *J. Geophys. Res. Planets*, 121, 338–352, doi:10.1002/2015JE004946.

Received 21 SEP 2015

Accepted 17 FEB 2016

Accepted article online 20 FEB 2016

Published online 12 MAR 2016

Observation of > 5 wt % zinc at the Kimberley outcrop, Gale crater, Mars

J. Lasue^{1,2}, S. M. Clegg³, O. Forni^{1,2}, A. Cousin^{1,2}, R. C. Wiens⁴, N. Lanza⁴, N. Mangold⁵, L. Le Deit⁵, O. Gasnault^{1,2}, S. Maurice^{1,2}, J. A. Berger⁶, K. Stack⁷, D. Blaney⁷, C. Fabre⁸, W. Goetz⁹, J. Johnson¹⁰, S. Le Mouélic⁵, M. Nachon⁵, V. Payré⁶, W. Rapin^{1,2}, and D. Y. Sumner⁷

¹IRAP, OMP, CNRS, Toulouse, France, ²IRAP, OMP, UPS, Toulouse, France, ³C-PCS, MS J565, Los Alamos National Laboratory, Los Alamos, New Mexico, USA, ⁴ISR, MS D466, Los Alamos National Laboratory, Los Alamos, New Mexico, USA, ⁵Laboratoire Planétologie et Géodynamique, LPGNantes, CNRS UMR 6112, Université de Nantes, Nantes, France, ⁶Department of Earth Sciences, University of Western Ontario, London, Ontario, Canada, ⁷Jet Propulsion Laboratory, California Institute of Technology, Pasadena, California, USA, ⁸GeoRessources, Lorraine University, CNRS, Vandoeuvre, France, ⁹Max Planck Institut für Sonnensystemforschung, Göttingen, Germany, ¹⁰The Johns Hopkins University, Applied Physics Laboratory, Laurel, Maryland, USA

Abstract Zinc-enriched targets have been detected at the Kimberley formation, Gale crater, Mars, using the Chemistry Camera (ChemCam) instrument. The Zn content is analyzed with a univariate calibration based on the 481.2 nm emission line. The limit of quantification for ZnO is 3 wt % (at 95% confidence level) and 1 wt % (at 68% confidence level). The limit of detection is shown to be around 0.5 wt %. As of sol 950, 12 targets on Mars present high ZnO content ranging from 1.0 wt % to 8.4 wt % (Yarrada, sol 628). Those Zn-enriched targets are almost entirely located at the Dillinger member of the Kimberley formation, where high Mn and alkali contents were also detected, probably in different phases. Zn enrichment does not depend on the textures of the rocks (coarse-grained sandstones, pebbly conglomerates, and resistant fins). The lack of sulfur enhancement suggests that Zn is not present in the sphalerite phase. Zn appears somewhat correlated with Na₂O and the ChemCam hydration index, suggesting that it could be in an amorphous clay phase (such as sauconite). On Earth, such an enrichment would be consistent with a supergene alteration of a sphalerite gossan cap in a primary siliciclastic bedrock or a possible hypogene nonsulfide zinc deposition where Zn, Fe, Mn would have been transported in a reduced sulfur-poor fluid and precipitated rapidly in the form of oxides.

1. Introduction

The Mars Science Laboratory (MSL) mission was selected to land at the bottom of Gale crater, Mars, a 154 km crater presenting a central mountain of flat-lying stratified rocks over 5 km, Aeolis Mons, also informally known as Mount Sharp. Gale crater is located at the boundary between the older and heavily cratered southern highlands and the more recent northern plains, with an estimated age ranging from 3.5 to 3.8 Ga, meaning that the sedimentary deposits probably date back to the late Noachian–early Hesperian eras of early Mars. Mount Sharp is assumed to consist of fill material deposited as sediments. From orbit, evidence of past water activity has been detected in the form of alluvial fans flowing from the crater rim, across the landing ellipse, and toward a topographic low at the base of Mount Sharp. Near-infrared spectra show an age progression where clay and hematite bearing strata and sulfate-bearing strata are separated by a likely anhydrous unconformity. For a review on the geology of Gale crater, please see *Anderson and Bell* [2010], *Thomson et al.* [2011], *Le Deit et al.* [2013], and references therein.

MSL is the first landed planetary mission to traverse and explore more than 10 km of an ancient habitable environment constituted of lacustrine, deltaic, and alluvial sedimentary deposits [Grotzinger et al., 2014, 2015a]. In this environment, primary igneous minerals from rocks of basaltic composition, generally representative of the crustal composition of the planet, were diagenetically altered to hydrated clay minerals, iron oxides, and minor chloride at a low lying lacustrine deposit named Yellowknife Bay [Ming et al., 2014; Vaniman et al., 2014]. MSL measurements showed that diagenesis occurred at moderate pH, low salinity, and under reducing conditions. These deposits have even preserved trace amounts of organic carbon [Freissinet et al., 2015]. Late-diagenetic cross-cutting fractures were then filled with hydrous and anhydrous calcium sulfate deposits [Grotzinger et al., 2014; Ming et al., 2014; Vaniman et al., 2014].

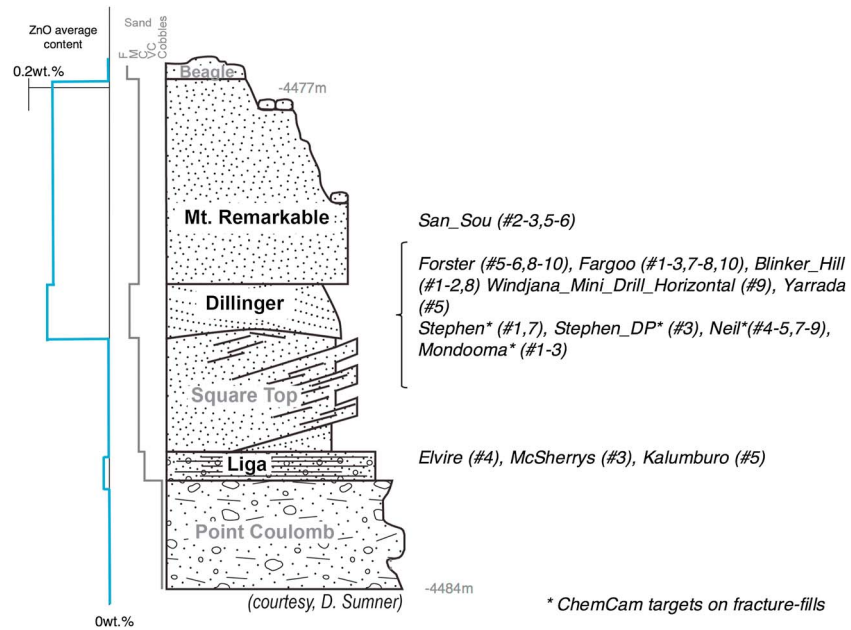


Figure 1. Stratigraphic column of the Kimberley formation with indications of grain size, member thickness, and elevation. The location of ChemCam targets in which Zn is detected (ZnO abundances above 0.5 wt % and confirmed with Zn emission lines) in the Kimberley formation is shown. The target named “Butchers_Gulley_hor” located on soil at the foot of the Kimberley formation is not indicated.

During the traverse, distinct chemical trends have become apparent, with a notable enrichment in alkali. Yellowknife Bay contains mudstones that are close to the average Mars crustal composition for most major elements [McLennan et al., 2014; Mangold et al., 2015a]. The nearby Shaler outcrop, which consists of alternating recessive and resistant cross-stratified sandstone, displays a range of compositions from close to the mudstone of Yellowknife Bay to more potassium rich [Anderson et al., 2015]. Across Bradbury Rise, a topographic rise that extends from the northern base of Mount Sharp to the distal end of the present-day Peace Vallis alluvial fan across the landing ellipse [Vasavada et al., 2014; Palucis et al., 2014], conglomerates [Williams et al., 2013; Mangold et al., 2015b], float rocks [Sautter et al., 2014, 2015], and even soils [Meslin et al., 2013; Cousin et al., 2015] displays unique enrichments of alkali and plagioclase feldspar compositions [Stolper et al., 2013; Schmidt et al., 2014]. The presence of silica- and feldspar-rich materials at Gale crater may sample low degrees of partial melting of the primitive Martian mantle analogous to the earliest continental crust found on Earth [Sautter et al., 2015].

Around sols 608 the Curiosity rover arrived at an outcrop informally named Kimberley, where three major geomorphologic units visible from orbit are exposed: light-toned striated rocks (southward dipping bedded sandstones referred to as the “Orbital Striated Outcrop” (OSO)), an overlying rugged unit, and the uppermost tonally smooth but hummocky unit (supporting information Figures S1 and S2) [Grotzinger et al., 2014, 2015a]. A composite stratigraphic column for the Kimberley formation shows the range in lithology from siltstone to conglomerates and the position of ChemCam targets (Figure 1). The Kimberley outcrop includes six members, in ascending stratigraphic order: the “Point Coulomb member,” the “Liga member” and the “Square Top member” (both associated with the striated unit), the “Dillinger member” and the “Mount Remarkable member” (associated with the rugged unit), and the “Beagle member” (S. Gupta et al., manuscript in preparation, 2016; L. Le Deit et al., The potassic sedimentary rocks in Gale crater, Mars, as seen by ChemCam on board Curiosity, submitted to *Journal of Geophysical Research*, 2016). These members range from relatively coarse to finer-grained sediments. The lowermost member, the Point Coulomb, is a conglomerate with poorly rounded pebbles. It is poorly stratified and likely had significant topography on top of it prior to the deposition of the overlying Liga member. The Liga member consists of planar-bedded granule conglomerate. The overlying Square Top member includes the southward dipping sandstones of the OSO and is overlain by the Dillinger member, which was the main focus of Curiosity’s drill and geochemistry analyses in this area. The Dillinger member consists of medium-grained to fine-grained stratified sandstones with low-angle cross bedding

representing a complex southwesterly mixed deposit alternating possibly fluvial and dry aeolian episodes of deposition (S. Gupta et al., manuscript in preparation, 2016; C. Lewis et al., manuscript in preparation, 2016). Furthermore, the Dillinger member is also cross cut by fractures containing Mn-rich resistant fin material that indicate a later stage water circulation within the member. The Dillinger member became the target for drilling at a site named Windjana (supporting information Figure S3). A third member, Mount Remarkable, is exposed in buttes overlying the other members. Due to inaccessibility, the Mount Remarkable member was only sampled by ChemCam. The Beagle member consists of float blocks on lower slopes.

Chemistry at the Kimberley outcrop proved to be anomalous in a number of respects. The region is especially rich in potassium [Le Deit et al., 2015; L. Le Deit et al., submitted manuscript, 2016], reflecting the substantial fraction of K feldspar (20 wt %) detected by the X-ray diffraction data from the CheMin instrument [Treiman et al., 2016]. Relatively abundant fluorine detections were made [Forni et al., 2015; O. Forni et al., manuscript in preparation, 2016], and the apparent fracture-filling material was found to contain high concentrations (>10 wt %) of manganese-oxide minerals (N. Lanza et al., Oxidation of manganese in an ancient aquifer, Kimberley formation, Gale crater, Mars, submitted to *Nature Geosciences*, 2016).

The Alpha-Particle X-ray Spectrometer (APXS), an elemental composition instrument located on the arm of MSL, made 26 measurements at Kimberley. It showed the outcrop to be strongly enriched in zinc from 283 to 8150 ppm [Berger et al., 2014; J. A. Berger et al., manuscript in preparation, 2016] and in copper especially the Liga and Dillinger members [Gellert et al., 2014; R. Gellert et al., manuscript in preparation, 2016]. ChemCam made more than 600 chemistry measurements at Kimberley, including measurements of common targets with APXS. Consistent with the APXS results, anomalous emission peaks observed within the ChemCam spectra were identified as zinc emission lines in the Windjana area. The ChemCam zinc observations and their context are reported here, compared with other MSL measurements, and discussed with respect to the potential origin of the Kimberley outcrop.

2. Zn Detection and Quantification With ChemCam

2.1. The ChemCam Instrument

ChemCam is a laser-induced breakdown spectroscopy (LIBS) instrument on board the MSL Curiosity rover. ChemCam analyzes the chemical composition of geological samples at a distance (1.56 to 7 m) by detecting the light emission of constituting elements in a plasma induced by the focused laser energy [Maurice et al., 2012; Wiens et al., 2012]. As the excited ions and atoms constituting the plasma relax to their ground state, they emit light at characteristic wavelengths from the ultraviolet to the visible and near infrared. The emitted photon energies are analyzed by spectrometry to determine the elemental composition of the target (for reviews, see Cremers and Radziemski [2006] and Miziolek et al. [2006], and references therein). ChemCam is sensitive to most chemical elements and can also be used to detect and quantify a set of minor and trace elements such as Li, Sr, Ba, and Rb [Ollila et al., 2014]; Mn [Lanza et al., 2014; N. Lanza et al., submitted manuscript, 2016]; and F [Forni et al., 2015; O. Forni et al., manuscript in preparation, 2016].

ChemCam emits 4.5 ns laser pulses ranging from 6.5 mJ to 14 mJ at the target. A typical point analysis acquires 30 spectra within 10 s. Each target is observed using a raster pattern (1 × 5, 1 × 10, 3 × 3, etc.). The spot size of the LIBS analysis ranges from ~350 μm at 1.2 m to ~550 μm at 7 m [Maurice et al., 2012]. For every target, a single shot removes about a microgram of material, or about 1 μm in depth. The plasma light is collected by a 110 mm diameter telescope and transmitted to three spectrometers that cover the 240 nm to 905 nm spectral range [Wiens et al., 2012]. The ChemCam spectrometers can also be used in passive mode, which provides reflectance spectra between 400 and 840 nm to assess the mineral composition of rocks [Johnson et al., 2015]. The LIBS instrument is complemented by a black and white Remote Microimager (RMI) with a resolution (2 pixels) of ~80 μm at 2 m and ~400 μm at 10 m [Le Mouélic et al., 2015]. Context imaging presented in this work is also provided by the Mast Camera (MastCam) instrument, a color imaging system based on a Bayer Pattern Filter CCD with a resolution of ~150 μm at 2 m [Grotzinger et al., 2012].

Zn has a relatively high ionization energy of 9.39 eV [Kramida et al., 2014], which is higher than typical elements detected by LIBS. The limit of detection (LOD) of this element using LIBS ranges from 100 to 400 ppm using optimized laboratory setups and the most intense lines at 481.2 nm, 330.4 nm, and 334.6 nm [Cremers and Radziemski, 2006, and references therein]. The ChemCam instrument was developed to detect

Table 1. ChemCam Zn Emission Lines, With Relative Intensity Estimation Obtained on Low-Density Sources [Kramida et al., 2014], Potential Interferences, Limits of Quantification (LOQ) at 95% of the Regression and Its Correlation Coefficient^a

	Wavelength (nm)	Ionized State	Relative Intensity	Interference	95% LOQ (ZnO wt %)	Correlation Coefficient
1	250.274	II	1000	-	6.6	0.96
2	255.872	II	1000	-	6.3	0.97
3	277.18	I	300	weak line	-	-
4	280.17	I	400	Mg II 279.6 nm Mg II 280.4 nm	-	-
5	303.666	I	200	Ti II 303 nm	-	-
6	307.295	I	200	Ti II 307.3 nm	-	-
7	307.679	I	150	Ti II 307.6 nm	-	-
8	328.328	I	500	-	7.1	0.95
9	330.353	I	800	Na II 330.2 nm	3.8	0.98
10	330.389	I	700	Na II 330.2 nm	3.8	0.98
11	334.598	I	800	Ti I 334.3 nm Ti II 335 nm	6.2	0.96
12	334.653	I	500	Ti I 334.3 nm Ti II 335 nm	6.2	0.96
13	468.145	I	300	Ti I 468.3 nm	8.0	0.92
14	481.187	I	400	Ti I 480.7 nm Ti I 482.2 nm	3.0	0.99
15	491.299	II	800	-	6.6	0.96
16	492.54	II	500	-	6.6	0.96
17	602.285	II	500	weak line	-	-
18	610.418	II	500	Ca I 610.4 nm	-	-
19	636.41	I	1000	Si II 637.3 nm	14.2	0.82
20	748.09	II	200	weak line	-	-
21	759.06	II	300	-	5.2	0.97
22	761.5	II	100	weak line	-	-
23	773.46	II	300	-	5.4	0.97
24	776	II	200	OI 777.6 nm	-	-

^aIn boldface are the lines that are used in this work for quantification or verification.

many elements, and Zn is expected to be detected only on the order of 1 wt % with this setup [Wiens et al., 2013]. The clear detection of Zn lines for target Yarrada (sol 628) indicating strong enrichment of this element in the Kimberley formation triggered the need to develop a specific calibration database for Zn.

2.2. Univariate Models for Zn Quantification With ChemCam

The first models developed for Zn quantification are based on single emission lines of the element detected in the spectra and qualified as univariate [Fabre et al., 2014]. The database for Zn quantification was developed at the Los Alamos National Laboratory with a twin setup of ChemCam analyzing targets under Martian conditions. We generated pressed pellet targets from ZnO powder intimately mixed with powdered Brammer geological standard basalt BHVO-2 (geological reference material from Brammer Standard Company containing 103 ppm Zn based on the U.S. Geological Survey Certificate of Analysis) [Wilson, 1997]. The team generated 10 calibrated standards with ZnO fractions of 0.1, 0.5, 1.1, 3.3, 5.0, 7.1, 11.0, 15.0, 30.0, and 100.0 wt % in a matrix that is close to the average Martian basaltic composition (see Table 1 in supporting information). It should be noted that since a single basaltic standard was mixed with ZnO, potential matrix effects may influence the quantification when applied to all the variety of rock compositions found at Gale crater.

Five locations are analyzed on each standard. The spectra are preprocessed and normalized to the total intensity per wavelength range [Wiens et al., 2013]. By comparing the spectra, the strength of the Zn emission lines and possible interferences by other elements can be assessed. The best emission lines for Zn detection and quantification are located around 330.4 nm, 334.6 nm, 468.1 nm, 481.2 nm, and 759.1 nm. A summary of all the Zn emission lines with their characteristics is given in Table 1, compiled from the National Institute of Standards and Technology database [Kramida et al., 2014]. Figure 2 shows the effect of increasing ZnO content in the 465–495 nm and 326–335 nm spectral regions. The limit of detection (LOD) of Zn is defined as the ZnO fraction for which the emission lines are detected above the 3σ background noise level of the spectrum. Figure 2 shows that the LOD value is between 0.5 wt % and 1 wt %.

A Voigt profile (a convolution of Gaussian and Lorentzian profiles) fit of the emission lines is used to calculate their area after local background subtraction and to generate a univariate regression model for the ZnO content.

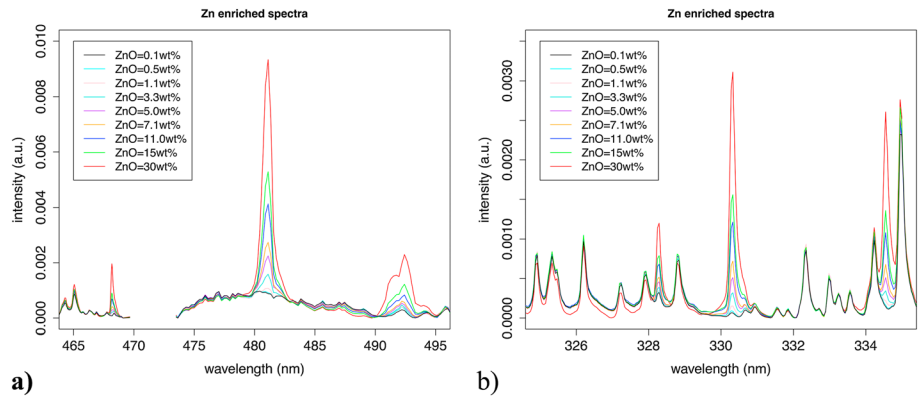


Figure 2. Plots of the Zn emission line intensity variations with the increase in ZnO content from 0.1 wt % to 30 wt %. (a) The spectral region 465–495 nm showing the major Zn lines at 468.1 nm and 481.2 nm. (b) The spectral region 326–335 nm showing the major Zn lines at 330.4 nm and 334.6 nm.

Similar procedures have been used to generate univariate models for ChemCam elemental quantification in previous works [Fabre et al., 2014; Ollila et al., 2014]. Figure 3 shows the regression models for the Zn emission line at 481.2 nm and 330.4 nm and for ZnO contents between 0 and 30 wt %. The regression line confidence limits are shown in green, and the 95% (2σ) confidence prediction limits in red. The upper confidence prediction limit crosses the y axis in y_0 . The 95% confidence limit of quantification (LOQ) is defined as the intersection of the horizontal line $y = y_0$ and the lower confidence prediction limit, which limits the false predictions to 5% or less (chapter 13 in Massart et al. [1998]). The LOQ of the 481.2 nm and 330.4 nm lines are 3.0 wt % (2σ), 1.0 wt % (1σ), and 3.8 wt % (2σ) and 1.2 wt % (1σ), respectively.

Table 1 includes the 2σ LOQ of linear regression models based on the Zn emission lines and the correlation coefficient. These values confirm the best emission lines for detection and quantification.

To confirm that Zn was present in targets analyzed by ChemCam, other Zn lines were checked. All targets that are defined to contain Zn present simultaneous emission lines above the detection level at 330.4 nm, 334.6 nm, 468.1 nm, 481.2 nm, and 759.1 nm.

2.3. Multivariate Model for Zn Quantification

It is possible to use multiple emission lines to improve the quantification of elemental composition with LIBS. This can be done for major elements [Clegg et al., 2009] as well as for minor elements [Ollila et al., 2014]. A partial least squares (PLS) model was generated using restricted regions of the processed spectra around the major Zn lines defined above: 330.4 nm, 334.6 nm, 468.1 nm, 481.2 nm, and 759.1 nm. The PLS model accuracy is defined by the cross-validation Root-Mean-Square of Error Prediction (RMSEP), which is statistically

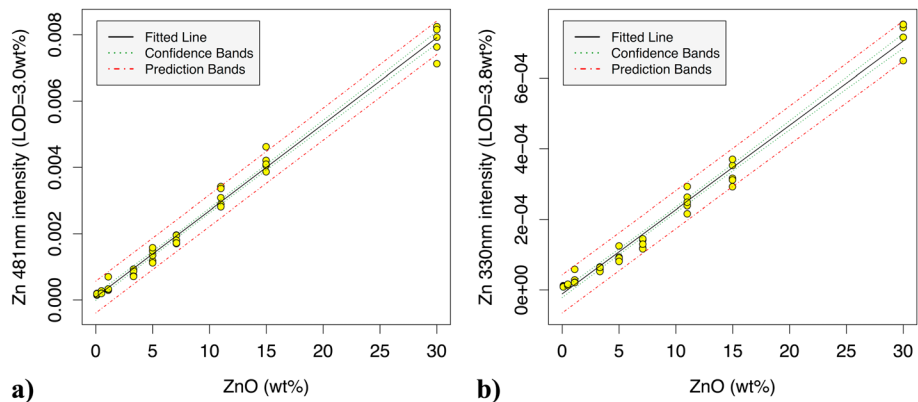


Figure 3. Regression models for the Zn emission lines. Green lines show the 95% confidence bands of the regression line, red lines show the 95% confidence bands for the ZnO prediction. (a) Regression model for the Zn emission line at 481.2 nm. (b) Regression model for the Zn emission line at 330.4 nm.

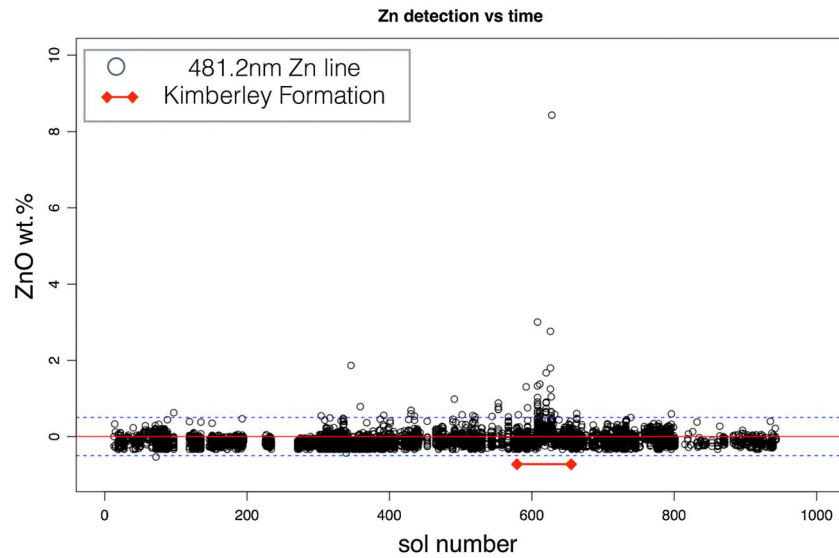


Figure 4. ZnO content (wt %) detected and quantified over time by ChemCam. A clear increase in the detection level of Zn is noticeable at the Kimberley formation (from sol 580 to sol 630). Rover paint detection is not shown. The highest ZnO content is in target Yarrada (sol 628). Shown as dashed lines are the limits at ± 0.5 wt % (corresponding to 2σ variations around 0).

similar to the univariate 1σ LOD. The RMSEP of the ZnO PLS model is 1 wt %, similar to the univariate 1σ LOD. Therefore, using PLS will not significantly improve Zn quantification. Moreover, the Zn abundances obtained with PLS are consistent with the 481.2 nm line univariate ones.

3. Zn-Rich Targets Detected by ChemCam on Mars

3.1. Zn-Rich Targets Analyzed by ChemCam

We have applied the Zn detection and quantification models on all data taken by ChemCam until sol 950. The initial detection is based on the diagnostic 481.2 nm emission line, which is not typically interfered with by contributions from other lines. We apply a threshold for the intensity and the position of the peak. Figure 4 shows the ZnO abundances as a function of sol number. Thirty-six locations out of 6784 are detected with a ZnO content of at least 0.5 wt %, and 12 locations have ZnO detections above 1 wt %. When considering the predicted abundances below the LOD of 1 wt %, their average is -0.09 wt %, and their 3σ value is 0.5 wt %, which is consistent with the LOD of 1 wt % determined independently using the univariate regression model. In the initial phase of the mission, around Yellowknife Bay, there was no clear detection of Zn by ChemCam. An increase in Zn is noticeable at the Kimberley formation as shown in Figure 4 (from sol 580 to sol 630). Zn abundances then fall mostly below the LOD afterward, in the analyses of rocks at the Pahrump Hills outcrop at the base of Mount Sharp (reached after sol 750 [Grotzinger *et al.*, 2015a]).

Apart from the data taken on the rover paint known to be Zn rich (sol 271), the most intense Zn lines correspond to the location #5 of target Yarrada (sol 628) in the Dillinger member of the Kimberley formation with about 8.4 wt % ZnO. Figure 5 describes the context of this target as well as the analysis of the paint between two ChemCam calibration targets and shows the spectral regions around the diagnostic Zn lines at 330.4 nm, 334.6 nm, 468.1 nm, and 481.2 nm.

Table 2 gives a summary of the data points with abundances above 1.0 wt % for which the clear presence of Zn has been confirmed using all Zn emission lines. A table detailing all the Zn detections with ZnO abundances above 0.5 wt % confirmed with diagnostic Zn peaks is given in the supporting information Table S2.

3.2. Zn-Rich Targets at the Kimberley Formation

The ChemCam Zn detections are mostly located within the Kimberley formation and surrounding area. Within the Kimberley formation, they are very well localized stratigraphically as indicated in Figure 1. Table 3 together with Figure 1 details the relationship between the Zn detections and the Kimberley formation stratigraphy, with an indication of the number of detections and an average Zn abundance for each member.

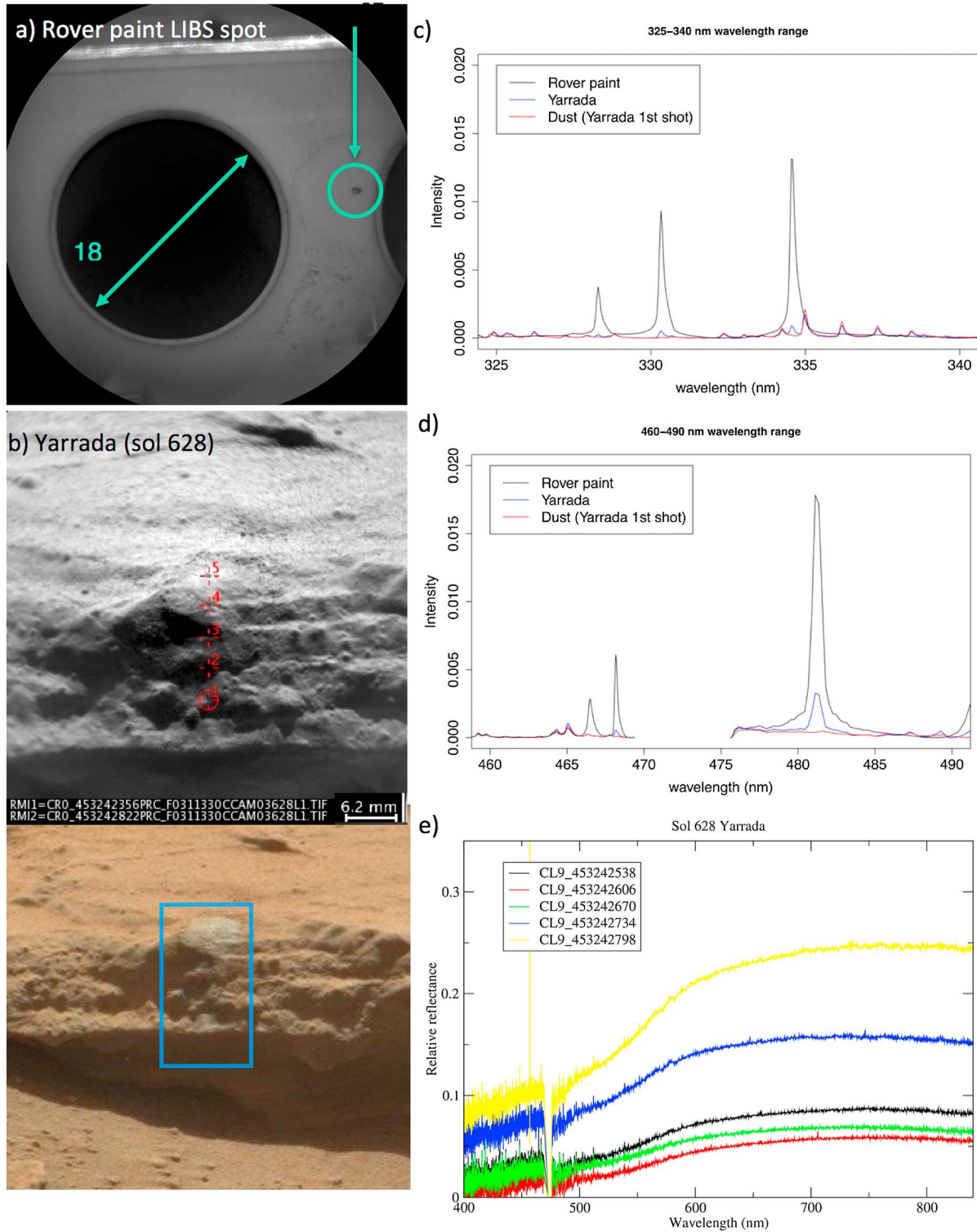


Figure 5. Martian targets with the strongest Zn enrichments. (a) Rover paint data point (RMI: 421727882PRC; sol 271). (b) Yarrada target (sol 628) Zn-enriched point is location #5 (RMI: 453242356PRC; 453242822PRC and MastCam MR002683 context images). (c and d) Comparison of the spectra for the rover paint, the first shot on Yarrada (Mars dust) and the average shots on Yarrada location #5 clearly showing the Zn lines at 330.4 nm, 334.6 nm, 468.1 nm, and 481.2 nm in these targets, which are absent in the Martian dust. (e) Passive spectra of all Yarrada locations in the visible and near-infrared region, showing the increased reflectance for location #5 (in yellow).

Table 2. ChemCam Targets Detected With ZnO Abundances Above 1 wt % and Confirmed With Other Zn Emission Lines at 330.4 nm, 334.6 nm, 468.1 nm, and 759.1 nm

Filename	Name	Outcrop	Unit	ZnO wt %	SiO ₂	TiO ₂	Al ₂ O ₃	FeOT	MgO	CaO	Na ₂ O	K ₂ O	Total
				(481.2 nm)									
428203528CCS	La_Reine			1.9	52.2	0.7	6.3	19.6	18.8	4.1	1.6	0.1	105.3
450044613CCS	Butchers_Gulley_hor	Kimberley	Soils	1.3	51.2	0.6	9.9	19.0	6.4	7.4	1.9	1.6	99.3
451464633CCS	Forster	Kimberley	Dillinger	1.0	41.2	0.8	7.7	17.6	7.6	10.1	1.3	3.0	90.3
451464698CCS	Forster	Kimberley	Dillinger	1.3	45.9	0.8	9.2	17.3	6.7	9.7	2.3	3.3	96.6
451464764CCS	Forster	Kimberley	Dillinger	3.0	45.3	0.8	8.7	19.3	8.0	6.8	2.4	3.1	97.1
451742911CCS	Blinker_Hill	Kimberley	Dillinger	1.4	44.0	0.8	7.5	17.8	11.1	4.8	1.7	2.3	91.3
452536353CCS	Neil	Kimberley	Mn-rich target	1.7	39.8	0.8	6.0	18.0	12.9	3.4	1.9	1.2	85.6
453063967CCS	Mondooma	Kimberley	Mn-rich target	1.8	40.7	0.8	6.8	17.5	13.4	3.1	3.1	1.7	88.5
453064043CCS	Mondooma	Kimberley	Mn-rich target	2.8	43.9	0.8	7.2	17.6	14.0	3.5	3.0	2.1	94.4
453064108CCS	Mondooma	Kimberley	Mn-rich target	1.2	44.1	0.8	8.0	18.5	12.2	3.9	2.1	3.0	93.8
453169841CCS	San_Sou	Kimberley	Mt. Remarkable	1.0	47.0	0.9	12.6	19.7	7.9	5.4	2.0	5.9	102.3
453242762CCS	Yarrada	Kimberley	Dillinger	8.4	47.2	0.9	8.1	17.5	9.4	3.0	4.4	1.9	100.2

Table 3 and supporting information Table S2 show that Zn is detected in rocks and soils of variable grain size and texture, with Zn-rich points detected in soils, granular, pebbly rocks, fine-grained sandstones, and resistant “fins” and fractures. The number of locations with Zn-rich targets is the highest in the two upper strata: Dillinger (fine sand sediment with Mn-rich fracture-fill diagenetic material; 28 locations) and Mount Remarkable (medium sand sediment; 4 locations) representing, respectively, 13 and 21% of the total locations analyzed by ChemCam in these two layers. The Liga member, a coarser interval dominated by pebbly sandstone and conglomerate, has three locations enriched in Zn indicating that Zn-rich points are not just restricted to the finer-grain rocks of the Kimberley formation.

If we consider that all locations with abundances lower than 0.5 wt % do not contain Zn and that the average analysis by ChemCam within a particular member is representative of its bulk composition (a strong assumption since the sampling may be biased), then the Dillinger member (219 ChemCam locations) has a mean ZnO abundance of about 0.17 wt % and the Mount Remarkable member (19 ChemCam locations) a mean of about 0.15 wt %, making their total average ZnO abundance comparable. Moreover, most locations with more than 1 wt % ZnO occur at the Dillinger member. The comparison between Dillinger member sedimentary bedrock analyses and data points taken on the diagenetic fracture fills indicates that both are comparable in terms of number of locations detected with Zn and average total ZnO content. It is notable that the relatively thick Square Top unit located between Dillinger and Liga, analyzed by ChemCam at 68 locations, does not seem to present any enhancement in Zn detectable by ChemCam.

Table 3. ChemCam Zn Abundances in the Kimberley Formation^a

Member	Locations	Locations With Zn	Percent of Locations With Zn	Average ZnO Abundances (wt %)	Average ZnO Total (wt %)
Beagle	16	0	0	-	-
Mt. Remarkable	19	4	21	0.7	0.15
Dillinger (all locations)	219	28	13	1.3	0.17
Dillinger (sediments)	156	15	10	1.5	0.14
Dillinger (fracture fills, Mn-rich)	63	13	21	1.1	0.23
Square_Top	68	0	0	-	-
Liga (all locations)	135	3	2	0.6	0.01
Liga-northern Kimberley	44	1	2	0.6	0.01
Liga-eastern Kimberley	45	1	2	0.8	0.02
Liga-southern Kimberley	26	0	0	-	-
Liga-south of Kimberley	20	1	5	0.6	0.03
Point_Coulomb	5	0	0	-	-
Soils	91	1	1	1.3	0.01

^aThe number of locations where Zn is detected is indicated. The average Zn abundance on the locations where detection occurred is given as average ZnO, and the total average Zn abundance on all locations analyzed at a given strata is given as ZnO average total.

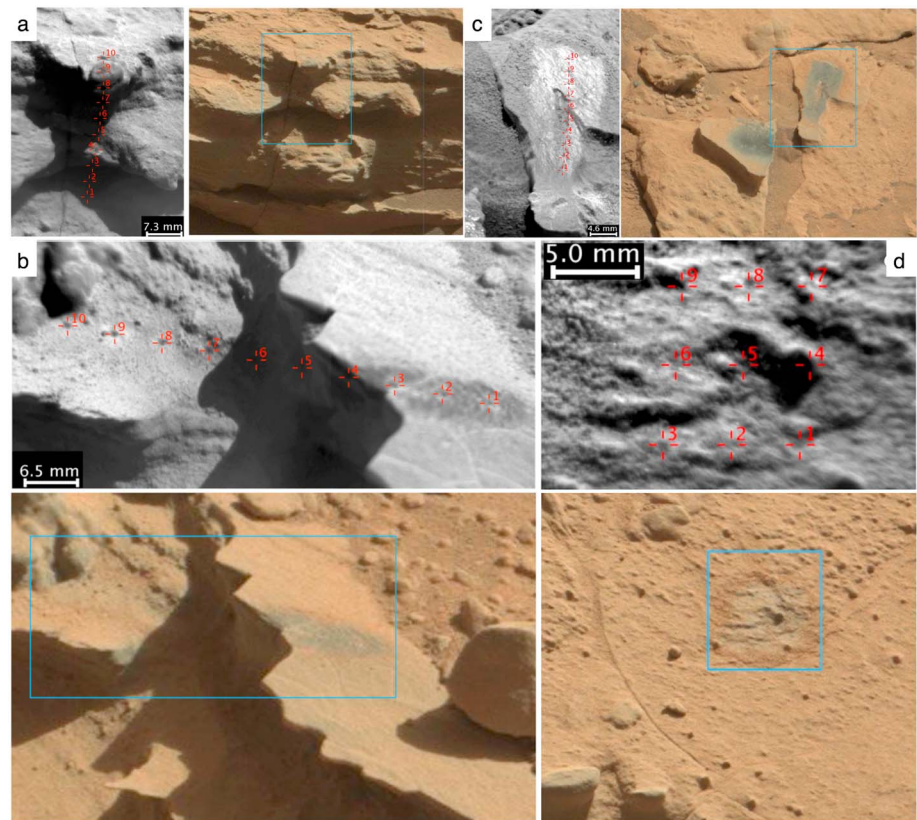


Figure 6. Zn-rich targets detected in the Dillinger member of the Kimberley formation. (a) Forster context images (451464823PRC; 451463816PRC and Mastcam MR002564). Zn is detected in locations #5 to #10, with abundances >1.0 wt % for the last three points. (b) Mondooma context images (RMI: 453063804PRC; 453064784PRC and Mastcam MR002679). Zn is detected in locations #1 to #3, with abundances >1.0 wt %. (c) Neil context images (RMI: 452535704PRC; 452536711PRC and Mastcam MR002676). Zn is detected in locations #4, #5, and #7–#9, with abundances >1.0 wt % for location #7. (d) Blinker_Hill context images (RMI: 451742081PRC; 451743034PRC and Mastcam MR002569). Zn is detected in locations #2 and #8, with abundance >1.0 wt % for the last point.

For more information regarding the stratigraphy of the Kimberley formation, please refer to M. Rice et al. (Overview of Kimberley Campaign, manuscript in preparation, 2016) and S. Gupta et al. (manuscript in preparation, 2016).

Yarrada location #5 clearly stands out as the ChemCam target with the highest content in ZnO detected to date in Gale crater. In Figure 5, geological context imaging is provided in black and white from the ChemCam RMI and in color from MastCam. From the context images (Figure 5), Yarrada #5 is located on a flat surface above the rock strata. Shot-to-shot analysis of the ChemCam data indicates that the first two shots are contaminated by overlying dust cover and are depleted in Zn. Below the dust, the rock is slightly hydrated, and Zn content is nearly constant over the remaining 28 shots taken at that location. ChemCam passive spectral analysis of location #5 at Yarrada shows a higher reflectance than other ChemCam targets without presenting any specific absorption feature (Figure 5).

The detections by ChemCam also show a strong Zn signal at depth on the shot-to-shot analyses. For example, at the Stephen target, a resistant fin fracture fill within the Dillinger member, a ChemCam depth profile of 150 shots taken at the same position on the rock was acquired to assess the variability of composition with depth [Lanza et al., 2014]. At this location (452535283CCS, Stephen_DP #3), Zn lines are clearly detected at an abundance of about 0.7 wt %. The strength of the Zn lines increases slightly with depth and decreases again, while the Mn content decreases as shot number increases, indicating that Zn and Mn may not be associated with the same mineral phase. The persistence of a strong Zn signal indicates that any coating containing Zn would be at least 100 μ m thick.

Other targets of the Dillinger unit that are strongly enriched in Zn with data points >1.0 wt % ZnO are Forster, Mondooma, Neil, and Blinker_Hill. Context RMI and Mastcam images are shown in Figure 6. For Forster, Zn is detected at locations #5, #6, and #8–#10, with abundances >1.0 wt % for the last three points. In this case, location #9 corresponds to a ~ 7 mm diameter nodule/pebble that is visibly different from the bedrock, but the Zn content and the major element composition appear to be quite similar to neighboring bedrock points analyzed (points 8 and 10), aside from a slight enhancement in Ca. The Mondooma target is a resistant fin protruding from the outcrop that is parallel to bedding, potentially Stephen like and high in Mn. Zn is detected on locations #1–#3, with abundances >1.0 wt %. Shot-to-shot analysis shows that Zn is present at all depths and Mn decreases with depth. Neil is another fin-like target enriched in Mn, which presents Zn at locations #5, #4, and #7–#9, with an abundance >1.0 wt % for location #7. The RMI images in Figure 6 show a bright specular reflection, which is consistent with featureless brighter passive spectra like that of Yarrada. Finally, Blinker_Hill is a granular pebbly outcrop near the Windjana drill target. It contains Zn at locations #1, #2, and #8, with abundance >1.0 wt % for the last point. Other analyses on pebbly bedrocks (e.g., in the Liga unit) do not show a specific correlation of Zn detection with pebbles. All the points containing Zn appear related to resistant edges of rocks.

4. Discussion

4.1. Comparison With APXS Measurements

The ChemCam Zn detections at the Kimberley formation and in the Dillinger member are consistent with the high detection of Zn in this area from the APXS measurements [Berger *et al.*, 2014; J. A. Berger *et al.*, manuscript in preparation, 2016]. The APXS is a precise contact elemental composition detection instrument with an aperture of ~ 1.7 cm that can detect elements with atomic numbers larger than Na. The depth sensitivity increases with atomic number, ranging from ~ 3 (Na) to ~ 90 μm (Fe) in a basaltic matrix, for example. Its LOD for Zn is of the order of 100 ppm. The APXS measurements at the Kimberley formation also indicate strong enrichment in Zn located at the Dillinger member on Windjana (3430–4680 ppm Zn) and on Stephen (~ 8150 ppm Zn), abundances that are consistent with ChemCam average measurements. Measurements made by APXS at other members in the Kimberley formation present a significantly lower Zn content than at Dillinger, with Square_Top around 1800 ppm, Liga around 937 ppm, and Lagrange around 283 ppm [Berger *et al.*, 2014; L. M. Thompson *et al.*, manuscript in preparation, 2016]. However, such values remain very high compared to average terrestrial igneous and sedimentary rocks compositions (50–80 ppm) [e.g., Wedepohl, 1995], as well as the shergottite, nakhlite, and chassigny classes of Martian meteorites compositional ranges (50–110 ppm) [e.g., Lodders, 1998] and previous in situ Martian rock analysis (40–570 ppm) [e.g., Gellert *et al.*, 2004]. Based on the ChemCam and APXS data sets, Zn detection is clearly enhanced in the Dillinger member. APXS was not deployed on the Mount Remarkable member of the Kimberley formation, limiting comparison of the two instruments to units below this member.

From the ChemCam measurements, Zn can be detected in a variety of rock textures and types and up to 100 μm in depth. The series of measurements made by APXS on Windjana include a raster on its surface detecting 3626 ppm Zn: a measurement made after brushing the surface of the rock giving 3981 ppm Zn and measurements made on the drill fines extracted from up to 6 cm depth and averaging 4311 ppm Zn. The variations in Zn content detected by both instruments from the surface of the rock suggest that Zn is not linked to a thin weathering layer or coating of the rock. This is unlike Mn, which was determined to be present in a layer much thinner than the LIBS depth profiles (about 100 μm) on the fin resistant edges (N. Lanza *et al.*, submitted manuscript, 2016). Moreover, as shown in Table 3, Zn is detected as often in Mn-rich and Mn-poor targets indicating an occurrence in a different phase and/or contrasting mobility in diagenetic fluids, Mn being more mobile than Zn. The associate enrichment of both elements in Stephen indicates conditions that mobilized and strongly enriched both elements in a fracture, such as low pH, high Eh fluid.

When comparing Zn with other elemental abundances observed at the ChemCam locations, there appears to be few correlations. Overall, the Zn-rich targets show a general enhancement in alkali (Na and K, which is quite high at Kimberley, from 1.9 to 5.3 wt % on average) [Le Deit *et al.*, 2015; L. Le Deit *et al.*, submitted manuscript, 2016]. The most robust correlation between the Zn abundance and other elements detected at Kimberley is with Na_2O (correlation value of 0.6) and H signal-to-background ratio (SBR; 0.2), which is an indicator of the hydrogen content of the target [Schroder *et al.*, 2015]. Weak anticorrelations may be observed with K_2O (-0.2) and CaO (-0.2). The correlations measured by ChemCam are given in Table 4, and the most

Table 4. Correlation Factors Between the Abundances of Zn and Other Elements Measured by ChemCam in the Kimberley Formation

ZnO Correlation	H SBR	SiO ₂	TiO ₂	Al ₂ O ₃	FeOT	MgO	CaO	Na ₂ O	K ₂ O
ChemCam values	0.2	0.1	0.2	-0.1	0.0	0.1	-0.2	0.6	-0.2

significant are plotted in Figure 7. In the APXS data set, Zn appears to be also strongly correlated with Mg, Mn, and minor species like Cl, Cu, Ni, and Br [Gellert *et al.*, 2014]. Ge detection was also made by APXS in correlation with the Zn enrichments at the Kimberley outcrop [Berger *et al.*, 2015]. Note that the sampling considerations of the instruments are very different, which may explain some apparent discrepancies. In particular, the ChemCam LIBS analyzes much smaller spots than the APXS field of view, and the arm deployment of APXS limits the number of measurements to a fraction of those capable by ChemCam in a reasonable amount of time given for investigating an outcrop. The detailed compositional values are given in supporting information Table 2.

4.2. Absence of a Sphalerite Phase

The detections of Zn in the bedrock could be either present in the deposited minerals or as a cement of the sedimentary layer. In igneous minerals, zinc may be present in pyroxenes by substitution for Fe²⁺ and Mg²⁺. Pyroxene is an abundant mineral at Kimberley in the form of augite (17 wt %), pigeonite (12 wt %), and orthopyroxene (2 wt %), as estimated from CheMin analyses [Treiman *et al.*, 2016]. Interestingly, a variety of augite rich in manganese and zinc called jeffersonite Ca(Mn,Zn,Fe)Si₂O₆ was found in the Franklin District, Sussex Co., New Jersey and surrounding areas [Palache, 1935]. However, ZnO abundances are typically limited below 0.1 wt % in these minerals and can hardly explain the observed enrichments in various contexts. Moreover, the Zn substitution of Mg and Fe ions would imply a positive correlation between Zn and Ca abundances, whereas in Kimberley sediments, they are weakly uncorrelated in ChemCam and APXS data sets (Figure 7 and Table 4), and Zn is not particularly uncorrelated with Fe or Mg. It is therefore

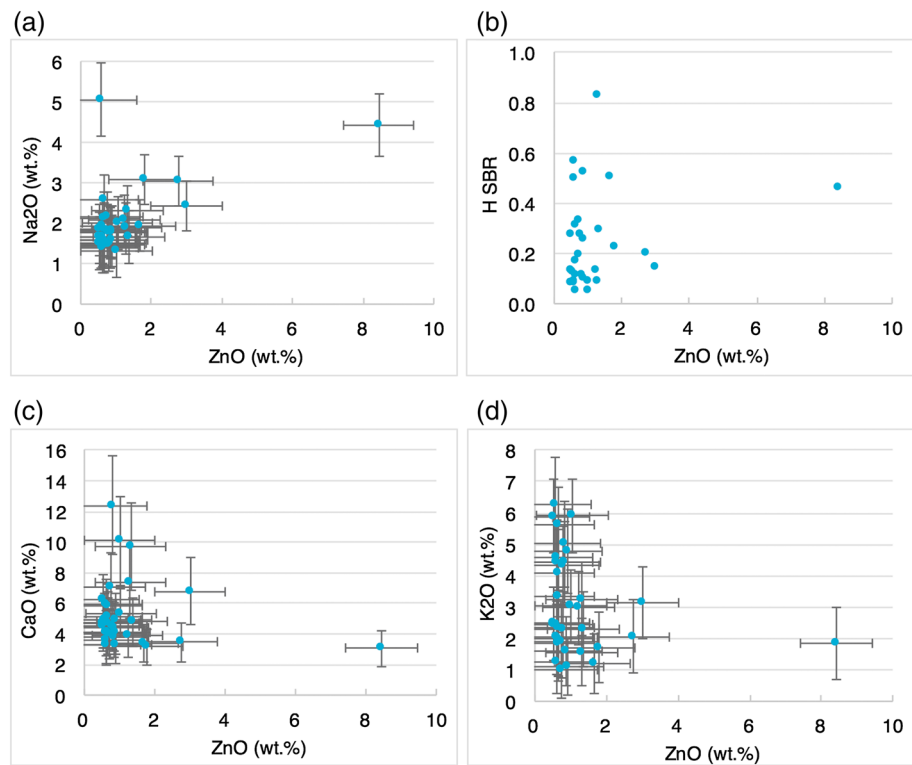


Figure 7. Apparent correlation between ZnO (>0.5 wt %) abundances at Kimberley and other elements. (a) Correlation with Na₂O (wt %) abundances from ChemCam. (b) Weak correlation with H content index from ChemCam [Schröder *et al.*, 2015]. (c and d) Weak anticorrelation with CaO and K₂O (wt %) abundances from ChemCam.

unlikely that Zn is present in a pyroxene phase. This could argue for the presence of Zn in a cement that would have been emplaced during the deposition or later circulation of water percolating through the rock from the surface.

The enrichment of Zn in the Dillinger member is also linked to an overall increase in Mn, Na, and K content. Given the high abundance of Mn coupled with the relevant appearance and high abundance of numerous trace metals (such as Co, Ba, and Ni and to a lesser extent Zn and Cu [Gellert *et al.*, 2014; Goetz *et al.*, 2016; Payré *et al.*, 2016]), it was inferred that Mn detected at Dillinger was present in a Mn-oxide phase. The association of Zn with Mn in some targets may indicate scavenging by the Mn oxide. To form such a phase would require oxidizing conditions and liquid water at typically higher pH range circulating through the Dillinger member (N. Lanza *et al.*, submitted manuscript, 2016).

On Earth, such high contents in Zn are associated with the Zn sulfide sphalerite in zinc ores, which is its main occurrence [Ridley, 2013]. Based on ChemCam, there is no clear detection of S in the Zn-enriched targets (SO_3 content below 5–10 wt %) [Nachon *et al.*, 2014, 2015], and SO_3 measured by APXS (LOD ~ 0.2 wt %) is not enhanced at Kimberley (R. Gellert *et al.*, manuscript in preparation, 2016) and appears anticorrelated with Zn. Therefore, the Zn-enriched targets probably do not contain sphalerite.

4.3. Possible Origin as a Nonsulfide Zinc Deposit

On Earth, nonsulfide zinc deposits usually are formed by supergene (water circulation and formation near the surface) or hypogene (water circulation and formation at depth) processes. While supergene deposits are the most common type of nonsulfide zinc deposit, they mostly occur by replacement of Zn sulfides in carbonate host rocks through the reaction of carbonate minerals with acidic, oxidized, zinc-rich fluids derived from the destruction of sphalerite-bearing sulfide bodies [Hitzman *et al.*, 2003]. The Kimberley outcrop does not present evidence of carbonate minerals from the CheMin mineralogical analysis [Treiman *et al.*, 2016], and there are no detections of C above atmospheric levels in the ChemCam data. This indicates that Zn is probably not present as a carbonate phase (such as smithsonite (ZnCO_3) or hydrozincite ($\text{Zn}_5(\text{CO}_3)_2(\text{OH})_6$)). However, another common mineral found in supergene deposits is sauconite ($\text{Na}_{0.3}\text{Zn}_3\text{Si}_3\text{AlO}_{10}(\text{OH})_2 \cdot 4(\text{H}_2\text{O})$, International Mineralogical Association), which is typical of deposits commonly associated with siliciclastic sedimentary materials such as the Skorpion supergene zinc deposit, Southern Namibia [Large, 2001; Borg *et al.*, 2003], or the Yanque supergene zinc deposit in Peru [Mondillo *et al.*, 2014]. Considering the correlation between Zn, Na, and hydration signals at Kimberley, it is quite possible that Zn occurs in such a phase (or an amorphous phase of this clay). New studies, however, indicate that sauconite is probably a mixture of several Zn clays, and Na may not always be present [Mondillo *et al.*, 2015]. It would be consistent with supergene leaching of sulfur deposits located at higher levels of the stratigraphy, and the Mount Remarkable and Dillinger members would represent the transition zone to a barren gossan. In such a model, the gossan cap, now removed from the outcrop, would have included sulfide bodies enriched in Zn. Water circulation and weathering could have generated secondary products to deposit as replacement, or in open space filling/fracture filling. This would be consistent with the observation of Zn enrichments both in the bedrock and in the resistant fins. It would necessitate several episodes of oxidizing fluid circulations to deposit the bulk Zn products and at a later stage the Mn-oxide products, which are found predominantly in the resistant fins. This supergene formation can be consistent with APXS-correlated detection of Ge with Zn at Gale crater [Berger *et al.*, 2015] that could originate from the weathering of Ge-rich sphalerites. Finally, this model would also be consistent with the metasomatism origin of the high abundances of K feldspar (16 wt %) in Windjana measured by the CheMin instrument [Treiman *et al.*, 2016].

An alternative scenario would consist of hypogene nonsulfide zinc deposits. These are rarer and include replacement deposits (that contain sphalerite), but also manganese rich, possibly exhalative stratiform bodies, that could also bear resemblance to the compositions seen at Kimberley. The stratiform, manganese-rich, nonsulfide zinc deposits appear to form primarily under reduced, low temperature to moderate temperature (80°–200°C), zinc-rich, sulfur-poor fluid mixing with an oxidized, sulfur-poor fluid [Hitzman *et al.*, 2003]. Hypogene nonsulfide zinc can occur in manganese-rich, stratiform deposits of willemite (Zn_2SiO_4), associated with Zn oxides like franklinite ($(\text{Zn}, \text{Mn}^{2+}, \text{Fe}^{2+})(\text{Fe}^{3+}, \text{Mn}^{3+})_2\text{O}_4$) or zincite ($(\text{Zn}, \text{Mn}^{2+})\text{O}$). One of the best examples is the Franklin and Sterling Hill zinc mines in New Jersey [Johnson and Skinner, 2003], but zinc oxides require high temperatures and metamorphism of the rocks to occur [Boni *et al.*, 2011], which is inconsistent with the measurements made at Kimberley indicating relatively low temperature diagenesis. Recent geochemical

modeling has demonstrated that willemite, instead of sphalerite, can precipitate from fluids exceeding 150°C with a low activity of sulfur and a relatively high oxygen fugacity [Brugger *et al.*, 2003]. A sulfate-poor oxidized fluid, at low temperatures, can transport significant quantities of Zn, Pb, or Cu. However, it would not transport much Fe or Mn and thus would be poorly associated with Mn enrichments. Seeing that the Dillinger member of the Kimberley formation also includes fracture-fill Mn and Cu enrichments, other episodes of oxidized fluid circulation may have had to happen through time, with the latest being the deposition of Mn-oxide coatings. Such deposits are also found on Earth in the Red Sea brine pools with base metal-rich clays and oxyhydroxides deposits [Degens and Ross, 2013]. Conditions for brine deposition could have been met at early Gale crater where standing bodies of water over 10,000 to 10 million years have been necessary to deposit the 75 m of sedimentary stratigraphy explored by MSL [Grotzinger *et al.*, 2015b]. Hydrothermal deposits would be consistent with APXS-correlated detection of Ge with Zn enrichment in Gale crater [Berger *et al.*, 2015]. However, the detection of olivine (5 wt %) in the mineralogy from the X-ray diffraction CheMin results at Windjana would argue for limited hydrothermal alteration of the bedrock [Treiman *et al.*, 2016]. Overall, the measurements made at Kimberley tend to favor a supergene deposit for the origin of the zinc enrichment.

5. Conclusions

High Zn content targets have been detected and quantified on Mars using the ChemCam instrument at the Kimberley formation. We have developed a dedicated calibration set to quantify the Mars Zn detections based on the 481.2 nm emission line. The ChemCam limit of quantification for ZnO is 3 wt % (95% confidence level) and 1 wt % (68% confidence level). The ChemCam limit of detection is around 0.5 wt % ZnO. As of sol 950, about 12 targets on Mars present ZnO contents ranging from 1.0 wt % to 8.4 wt % (Yarrada, sol 628). Those Zn-enriched targets are almost entirely localized at the Dillinger member of the Kimberley formation, where high Mn and alkali contents were also detected, but probably in different phases.

Zn enrichment does not correlate with the textures of the rocks as it is found in fine- to coarse-grained sandstones, pebbly conglomerates, and in resistant fins that cross cut the bedrock. Zn is also detected at various depths probed by ChemCam and APXS, indicating that this is probably not just a surficial addition. The lack of sulfur enhancement suggests that Zn is not present in the sphalerite phase. Zn appears to be somewhat correlated with Na₂O and the ChemCam hydration index, suggesting that it could be in an amorphous clay phase (such as sauconite). On Earth, such an enrichment would be consistent with a supergene alteration of a sphalerite gossan cap in a primary siliciclastic bedrock, with secondary products being deposited as replacements or in fracture fills. Several episodes of oxidizing water circulation are necessary to explain the presence of Mn oxides. It is also possible that a hypogene nonsulfide zinc deposition occurred where Zn, Fe, Mn would have been transported in a reduced sulfur-poor fluid, which could have precipitated rapidly in the form of zinc oxides if it encountered an oxidized solution.

Acknowledgments

The authors acknowledge fruitful discussions with Ralf Gellert. We are grateful to C.A. Johnson, P. Giesting, and M. Boni for very constructive and useful comments which helped significantly improve the manuscript. Funding for MSL and ChemCam operations and science in the U.S. was provided by the NASA Mars Exploration Program. Funding for ChemCam operations in France was provided by CNES; science funding in France was provided by CNRS. The authors gratefully acknowledge the support of all of the people at JPL involved in making MSL a successful mission. The data used in this study were generated by the ChemCam and the Mars Science Laboratory teams and are freely available at the Planetary Data System of NASA (<https://pds.jpl.nasa.gov/>). All data described in the text are indicated together with the spacecraft clock and three letters that describe the type of data used, which singly identify the data in PDS.

References

- Anderson, R. B., and J. F. Bell III (2010), Geologic mapping and characterization of Gale crater and implications for its potential as a Mars Science Laboratory landing site, *Mars*, 5, 76–128.
- Anderson, R., et al. (2015), ChemCam results from the Shaler outcrop in Gale crater, *Mars*, *Icarus*, 249, 2–21.
- Berger, J. A., M. E. Schmidt, R. Gellert, and M. R. Fisk (2014), Zinc enrichments in the rocks of Gale crater, Mars measured by MSL-APXS reflect both high Zn in Jake_M rocks and the concentration of Zn in sedimentary cements, Abstract P51E-3988 presented at 2014 Fall Meeting, AGU, San Francisco, Calif., Dec.
- Berger, J. A., et al. (2015), Germanium enrichments in sedimentary rocks in Gale crater, Mars: Constraining the timing of alteration and character of the protolith, *Lunar Planet. Sci. Conf.*, vol. 46, p. 1564.
- Boni, M., R. Terracciano, G. Balassone, S. A. Gleeson, and A. Matthews (2011), The carbonate-hosted willemite prospects of the Zambezi Metamorphic Belt (Zambia), *Miner. Deposita*, 46(7), 707–729.
- Borg, G., K. Kärner, M. Buxton, R. Armstrong, and S. W. van der Merwe (2003), Geology of the Skorpion supergene zinc deposit, southern Namibia, *Econ. Geol.*, 98(4), 749–771.
- Brugger, J., D. C. McPhail, M. Wallace, and J. Waters (2003), Formation of willemite in hydrothermal environments, *Econ. Geol.*, 98(4), 819–835.
- Clegg, S. M., E. Sklute, M. D. Dyar, J. E. Barefield, and R. C. Wiens (2009), Multivariate analysis of remote laser-induced breakdown spectroscopy spectra using partial least squares, principal component analysis, and related techniques, *Spectrochim. Acta, Part B*, 64(1), 79–88.
- Cousin, A., et al. (2015), Compositions of coarse and fine particles in Martian soils at Gale: A window into the production of soils, *Icarus*, 249, 22–42.
- Creemers, D. A., and L. J. Radziemski (2006), *Handbook of Laser-Induced Breakdown Spectroscopy*, John Wiley, Chichester, Engl.
- Degens, E. T., and D. A. Ross (2013), *Hot Brines and Recent Heavy Metal Deposits in the Red Sea: A Geochemical and Geophysical Account*, Springer, Verlag.
- Fabre, C., et al. (2014), In situ calibration using univariate analyses based on the onboard ChemCam targets: First prediction of Martian rock and soil compositions, *Spectrochim. Acta, Part B*, 99, 34–51.
- Forni, O., et al. (2015), Fluorine and lithium at the Kimberley outcrop, Gale crater, *Lunar Planet. Sci. Conf.*, XLVI.

- Freissinet, C., et al. (2015), Organic molecules in the Sheepbed mudstone, Gale crater, Mars, *J. Geophys. Res. Planets*, *120*, 495–514.
- Gellert, R., et al. (2004), Chemistry of rocks and soils in Gusev Crater from the Alpha Particle X-ray Spectrometer, *Science*, *305*(5685), 829–832.
- Gellert, R., et al. (2014), APXS chemical composition of the Kimberley sandstone in Gale crater, Abstract P34A-05 presented at 2014 Fall Meeting, AGU, San Francisco, Calif., Dec.
- Goetz, W., et al. (2016), Copper along the traverse of the Curiosity rover, Gale crater, Mars, Lunar Planet. Sci. Conf., XLVII.
- Grotzinger, J. P., et al. (2012), Mars Science Laboratory mission and science investigation, *Space Sci. Rev.*, *170*(1–4), 5–56.
- Grotzinger, J. P., et al. (2014), A habitable fluvio-lacustrine environment at Yellowknife Bay, Gale crater, Mars, *Science*, *343*(6169), doi:10.1126/science.1242777.
- Grotzinger, J. P., J. A. Crisp, and A. R. Vasavada (2015a), Curiosity's mission of exploration at Gale crater, Mars, *Elements*, *11*(1), 19–26.
- Grotzinger, J. P., et al. (2015b), Deposition, exhumation, and paleoclimate of an ancient lake deposit, Gale crater, Mars, *Science*, *350*(6257), doi:10.1126/science.aac7575.
- Hitzman, M. W., N. A. Reynolds, D. F. Sangster, C. R. Allen, and C. E. Carman (2003), Classification, genesis, and exploration guides for nonsulfide zinc deposits, *Econ. Geol.*, *98*(4), 685–714.
- Johnson, C. A., and B. J. Skinner (2003), Geochemistry of the furnace magnetite bed, Franklin, New Jersey, and the relationship between stratiform iron oxide ores and stratiform zinc oxide-silicate ores in the New Jersey highlands, *Econ. Geol.*, *98*(4), 837–854.
- Johnson, J. R., et al. (2015), ChemCam passive reflectance spectroscopy of surface materials at the Curiosity landing site, Mars, *Icarus*, *249*, 74–92.
- Kramida, A., Y. Ralchenko, J. Reader, and NIST ASD Team (2014), NIST atomic spectra database (ver. 5.2), National Institute of Standards and Technology, Gaithersburg, Md. [Available at <http://physics.nist.gov/asd>.]
- Lanza, N. L., et al. (2014), High manganese concentrations in rocks at Gale crater, Mars, *Geophys. Res. Lett.*, *41*, 5755–5763, doi:10.1002/2014GL060329.
- Large, D. (2001), The geology of non-sulphide zinc deposits—An overview zinc-exploration-calamine, *Erzmetall*, *54*(5), 264–274.
- Le Deit, L., E. Hauber, F. Fueten, M. Pondrelli, A. P. Rossi, and R. Jaumann (2013), Sequence of infilling events in Gale crater, Mars: Results from morphology, stratigraphy, and mineralogy, *J. Geophys. Res. Planets*, *118*, 2439–2473, doi:10.1002/2012JE004322.
- Le Deit, N., et al. (2015), The potassic sedimentary rocks in Gale crater, Mars as seen by ChemCam onboard Curiosity, Lunar Planet. Sci. Conf. XLVI, Abstract 1438.
- Le Mouélic, S., et al. (2015), The ChemCam remote micro-imager at Gale crater: Review of the first year of operations on Mars, *Icarus*, *249*, 93–107, doi:10.1016/j.icarus.2014.05.030.
- Lodders, K. (1998), A survey of shergottite, nakhlite and chassigny meteorites whole-rock compositions, *Meteorit. Planet. Sci.*, *33*(S4), A183–A190.
- Mangold, N., et al. (2015a), Chemical variations in Yellowknife Bay formation sedimentary rocks analyzed by ChemCam on board the Curiosity rover on Mars, *J. Geophys. Res. Planets*, *120*, 452–482, doi:10.1002/2014JE004681.
- Mangold, N., L. Thompson, L. Le Deit, O. Forni, R. Gellert, J. Grotzinger, S. Maurice, R. Wiens, and the ChemCam and APXS Curiosity teams Team (2015b), The chemistry of fluvial sediments analyzed by the Curiosity rover, EGU General Assembly Conference, 17, EGU2015-3839.
- Massart, D. L., B. G. M. Vandginste, L. M. C. Buydens, S. De Jong, P. J. Lewi, and J. Smeyers-Verbeke (Eds.) (1998), *Handbook of Chemometrics and Qualimetrics: Part A*, Elsevier, New York.
- Maurice, S., et al. (2012), The ChemCam instrument suite on the Mars Science Laboratory (MSL) rover: Science objectives and mast unit description, *Space Sci. Rev.*, *170*(1–4), 95–166.
- McLennan, S. M., et al. (2014), Elemental geochemistry of sedimentary rocks at Yellowknife Bay, Gale crater, Mars, *Science*, *343*(6169), doi:10.1126/science.1244734.
- Meslin, P. Y., et al. (2013), Soil diversity and hydration as observed by ChemCam at Gale crater, Mars, *Science*, *341*(6153), doi:10.1126/science.1238670.
- Ming, D. W., et al. (2014), Volatile and organic compositions of sedimentary rocks in Yellowknife Bay, Gale crater, Mars, *Science*, *343*(6169), doi:10.1126/science.1245267.
- Miziolek, A. W., V. Palleschi, and I. Schechter (Eds) (2006), *Laser-Induced Breakdown Spectroscopy (LIBS) Fundamentals and Applications*, Cambridge Univ. Press, New York.
- Mondillo, N., M. Boni, G. Balassone, and I. M. Villa (2014), The Yanque prospect (Peru): From polymetallic Zn-Pb mineralization to a nonsulfide deposit, *Econ. Geol.*, *109*(6), 1735–1762.
- Mondillo, N., F. Nieto, and G. Balassone (2015), Micro- and nano-characterization of Zn-clays in nonsulfide supergene ores of southern Peru, *Am. Mineral.*, *100*(11–12), 2484–2496.
- Nachon, M., et al. (2014), Calcium sulfate veins characterized by ChemCam/Curiosity at Gale crater, Mars, *J. Geophys. Res. Planets*, *119*, 1991–2016, doi:10.1002/2013JE004588.
- Nachon, M., et al. (2015), Diagenetic features analyzed by ChemCam/Curiosity at Pahrump Hills, Gale crater, Mars, Lunar Planet. Sci. Conf., vol. 46, p. 1524.
- Ollila, A. M., et al. (2014), Trace element geochemistry (Li, Ba, Sr, and Rb) using Curiosity's ChemCam: Early results for Gale crater from Bradbury landing site to Rocknest, *J. Geophys. Res. Planets*, *119*, 255–285, doi:10.1002/2013JE004517.
- Palache, C. (1935), *The Minerals of Franklin and Sterling Hill*, vol. 180, U.S. Government Printing Office, Sussex County, N. J.
- Palucis, M. C., et al. (2014), The origin and evolution of the Peace Vallis fan system that drains to the Curiosity landing area, Gale crater, Mars, *J. Geophys. Res. Planets*, *119*, 705–728, doi:10.1002/2013JE004583.
- Payré, V., et al. (2016), Copper detection in Gale crater: First calibration and quantification using ChemCam data, Lunar Planet. Sci. Conf. XLVII.
- Ridley, J. (2013), *Ore Deposit Geology*, Cambridge Univ. Press, New York.
- Sautter, V., et al. (2014), Igneous mineralogy at Bradbury Rise: The first ChemCam campaign at Gale crater, *J. Geophys. Res. Planets*, *119*, 30–46, doi:10.1002/2013JE004472.
- Sautter, V., et al. (2015), In situ evidence for continental crust on early Mars, *Nat. Geosci.*, *8*(8), 605–609.
- Schmidt, M. E., et al. (2014), Geochemical diversity in first rocks examined by the Curiosity rover in Gale crater: Evidence for and significance of an alkali and volatile-rich igneous source, *J. Geophys. Res. Planets*, *119*, 64–81, doi:10.1002/2013JE004481.
- Schröder, S., et al. (2015), Hydrogen detection with ChemCam at Gale crater, *Icarus*, *249*, 43–61.
- Stolper, E. M., et al. (2013), The petrochemistry of Jake_M: A Martian mugearite, *Science*, *341*(6153), doi:10.1126/science.1239463.
- Thomson, B. J., N. T. Bridges, R. Milliken, A. Baldridge, S. J. Hook, J. K. Crowley, G. M. Marion, C. R. de Souza Filho, A. J. Brown, and C. M. Weitz (2011), Constraints on the origin and evolution of the layered mound in Gale crater, Mars using Mars Reconnaissance Orbiter data, *Icarus*, *214*(2), 413–432.
- Treiman, A. H., et al. (2016), Mineralogy, provenance, and diagenesis of a potassic basaltic sandstone on Mars: CheMin X-ray diffraction of the Windjana sample (Kimberley area, Gale crater), *J. Geophys. Res. Planets*, *121*, 75–106, doi:10.1002/2015JE004932.

- Vaniman, D. T., et al. (2014), Mineralogy of a mudstone at Yellowknife Bay, Gale crater, Mars, *Science*, 343(6169), doi:10.1126/science.1243480.
- Vasavada, A. R., et al. (2014), Overview of the Mars Science Laboratory mission: Bradbury landing to Yellowknife Bay and beyond, *J. Geophys. Res. Planets*, 119, 1134–1161, doi:10.1002/2014JE004622.
- Wedepohl, K. H. (1995), The composition of the continental crust, *Geochim. Cosmochim. Acta*, 59(7), 1217–1232.
- Wiens, R. C., et al. (2012), The ChemCam instrument suite on the Mars Science Laboratory (MSL) rover: Body unit and combined system tests, *Space Sci. Rev.*, 170(1-4), 167–227.
- Wiens, R. C., et al. (2013), Pre-flight calibration and initial data processing for the ChemCam laser-induced breakdown spectroscopy instrument on the Mars Science Laboratory rover, *Spectrochim. Acta, Part B*, 82, 1–27.
- Williams, R. M., et al. (2013), Martian fluvial conglomerates at Gale crater, *Science*, 340(6136), 1068–1072.
- Wilson, S. A. (1997), Data compilation for USGS reference material BHVO-2, Hawaiian Basalt. U.S. Geol. Surv. Open File Rep.